



This is a repository copy of *A new potential for methylammonium lead iodide.*

White Rose Research Online URL for this paper:
<http://eprints.whiterose.ac.uk/110273/>

Version: Accepted Version

Article:

Handley, C.M. and Freeman, C.L. (2017) A new potential for methylammonium lead iodide. *Physical Chemistry Chemical Physics*, 19 (3). pp. 2313-2321. ISSN 1463-9076

<https://doi.org/10.1039/c6cp05829a>

Reuse

Unless indicated otherwise, fulltext items are protected by copyright with all rights reserved. The copyright exception in section 29 of the Copyright, Designs and Patents Act 1988 allows the making of a single copy solely for the purpose of non-commercial research or private study within the limits of fair dealing. The publisher or other rights-holder may allow further reproduction and re-use of this version - refer to the White Rose Research Online record for this item. Where records identify the publisher as the copyright holder, users can verify any specific terms of use on the publisher's website.

Takedown

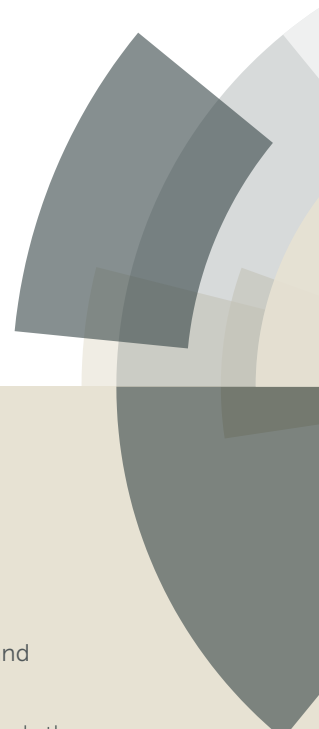
If you consider content in White Rose Research Online to be in breach of UK law, please notify us by emailing eprints@whiterose.ac.uk including the URL of the record and the reason for the withdrawal request.



eprints@whiterose.ac.uk
<https://eprints.whiterose.ac.uk/>

PCCP

Accepted Manuscript



This article can be cited before page numbers have been issued, to do this please use: C. M. Handley and C. L. Freeman, *Phys. Chem. Chem. Phys.*, 2016, DOI: 10.1039/C6CP05829A.



This is an Accepted Manuscript, which has been through the Royal Society of Chemistry peer review process and has been accepted for publication.

Accepted Manuscripts are published online shortly after acceptance, before technical editing, formatting and proof reading. Using this free service, authors can make their results available to the community, in citable form, before we publish the edited article. We will replace this Accepted Manuscript with the edited and formatted Advance Article as soon as it is available.

You can find more information about Accepted Manuscripts in the [author guidelines](#).

Please note that technical editing may introduce minor changes to the text and/or graphics, which may alter content. The journal's standard [Terms & Conditions](#) and the ethical guidelines, outlined in our [author and reviewer resource centre](#), still apply. In no event shall the Royal Society of Chemistry be held responsible for any errors or omissions in this Accepted Manuscript or any consequences arising from the use of any information it contains.



Journal Name

ARTICLE

A new potential for Methylammonium Lead Iodide

C. M. Handley^a and C. L. Freeman^{a†}Received 00th January 20xx,
Accepted 00th January 20xx

DOI: 10.1039/x0xx00000x

www.rsc.org/

We present a new set of interatomic potentials for modelling Methylammonium Lead Iodide. The potential model uses existing potentials for lead iodide and methylammonium, and new functions are fitted to enable these pre-existing potentials to be used together, while still be capable of modelling lead iodide and methylammonium iodide as separate materials. Fitting was performed using a combination of ab initio, and experimental reference data. The model is tested by simulating methylammonium lead iodide at a range of temperatures. Our simulations are in agreement with experiment and reveal the short and long range ordering of the molecular cations and lead iodide octahedra.

Introduction

MALI is an important discovery along the path of developing better photovoltaic devices, and is one of the most extensively studied hybrid halide perovskites. It is the focus of numerous experimental and computational studies, seeking to understand its properties better, how they may be tuned for greater efficiency, and to improve the manufacture of the material for incorporation into photovoltaic devices¹⁻⁴.

Hybrid metal halide perovskites are utilized in the production of solar cells, as an alternative to organic dyes⁵. However, the dye based systems cannot be manufactured as thin films, restricting their use in solid-state solar cells⁶. The need for thin films of less than 2 μm suitable for solid state solar cells⁷ has driven the use of alternative inorganic light absorbers, including hybrid metal halide perovskites⁸. The necessity to use of a liquid electrolyte in these new perovskite absorbers, as the perovskite is dissolved by ionic liquids⁹, led to their further development as solid-state perovskite solar cells, displaying power conversion efficiencies (PCEs) of 8% and 10% for MAPb_{1-x}Cl_x and MAPbI₃ respectively^{10,11}. The report by Kojima et al on the photovoltaic performance of the MAPbX₃ (X = Br, I) series dramatically changed the focus of the photovoltaic (PV) field¹².

PCEs of 13% have been achieved for liquid electrolyte based dye-sensitised solar cells (DSSCs)¹³, compared to a 7% for solid state DSSCs (ssDSSC)¹⁴. However, the perovskite solar cells present significant improvements by absorbing light over a wider spectrum, allowing for a more complete absorption and conversion of the incident light, within thin films of just 500nm to 2 μm. In previous ssDSSCs the thickness of these films was limited by the spiro-MeOTAD hole transport medium (≤ 2 μm) to 10 μm to achieve

significant solar adsorption².

The versatility of the perovskite structure known for oxides is also found for the halides. We consider here perovskites with the general formula of AMX₃, where A⁺ = Cs, CH₃NH₃, CH(NH₂)₂ etc, M²⁺ = Pb, Sn and X = I, Br, Cl. Many studies show that mixing the composition can improve the stability of the materials or tune the properties for better solar cell materials. The stability of CH₃NH₃PbI₃ (MALI) has been heavily studied using experimental and computational methods, however, there is very little mention of the synthesis mechanism.

Methylammonium lead iodide (MALI) is synthesised by the reaction of hexagonal layered PbI₂ and the organic halide CH₃NH₃I (MAI). Initial syntheses reported by Weber⁸ and Poglitsch¹⁵ were solution based methods using concentrated hydroiodic acid, lead acetate or lead nitrate, and methylamine.

MALI is one of a number of hybrid metal halide perovskites, a class of material that exhibits a wide range of structural diversity owing to the formation of corner-sharing octahedral sub-units within the crystal¹⁶. The A cation occupies a cuboctahedron cavity, where the vertices are the X anions. The X anions also form octahedral arrangements about the M cation. The formation of the perovskite is limited by the geometric tolerance factor, *t*, which is a measure determined from the relative ion sizes within the perovskite. In Eqn. 1 *r_a*, *r_m*, and *r_x* are the radii of each of the ions that form the perovskite

$$t = \frac{r_A + r_X}{\left[\sqrt{2(r_M + r_X)} \right]} \#1$$

For a stable perovskite, *t* is expected to fall within the range of 0.813-1.107 in the case of alkali metal halide based perovskites¹⁷, and 0.9-1.0 for hybrid metal halide perovskites¹⁸. Using the effective radii for the ions, Park et al. determined that the A-site cation would form a stable perovskite if it had an effective ionic radius of 1.6-2.5 Å². MA has an effective ionic radius of 1.8 Å^{19,20}, which results in a tolerance factor of 0.8. This predicts that the perovskite structure of MALI should not be cubic and a tetragonal structure has been reported at room temperatures.

^a Department of Materials Science and Engineering, University of Sheffield, Mappin Street, Sheffield, S1 3JD, UK.

† Email: c.l.freeman@sheffield.ac.uk

Electronic Supplementary Information (ESI) available: [details of any supplementary information available should be included here]. See DOI: 10.1039/x0xx00000x

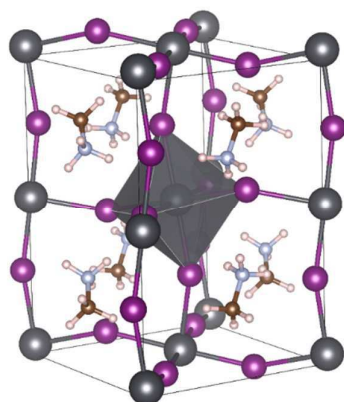


Figure 1 Unit cell of MALI. Atoms are coloured to denote lead (grey), iodide (purple), carbon (light grey), hydrogen (beige), and nitrogen (brown). The central PbI_6 octahedron is rendered.

Computationally, significant effort has been dedicated to understanding the band gap of these materials, and the structural and chemical influences upon them, in order to guide synthetic processes to tune this critical property²¹. The electronic properties of MALI are primarily determined by the iodine 5p orbitals that form the valence band, and the lead 6p orbitals which form the conduction band. The hybridization of these orbitals results in a valence band that consists of anti-bonding orbitals and a conduction band formed from the empty Pb p orbitals²². The band gap of MALI is 1.55-1.61 eV, determined by room temperature photoluminescence²³⁻²⁶, and is computationally predicted using a relativistic self-consistent quasiparticle GW method as 1.66-1.72 eV^{27,28}. Such calculations are required to account for the behaviour of the electrons about the heavy Pb and I ions, since the valence electrons experience significant relativistic effects²⁹ including spin-orbit coupling, which must be appropriately accounted for despite the fortuitous cancellation of errors if these corrections are neglected from calculations for determining the band gap^{30,31}.

The main role of the A-site cation in determining the band gap is how it controls the linearity of the I-Pb-I bonds. These perovskites consist of PbI_6 octahedra, connected together by corner shared I ions. Filip et al. determined from X-ray diffraction data that the Pb-I bonds are all of a similar length, displaying at most a 0.1% deviation from the 3.18 Å bond length^{32,33}. In addition, the PbI_6 octahedra have regular geometries, where the octahedral diagonals are near-perfectly aligned perpendicular to each other, with a maximum distortion from the ideal right angles of 4°. The manner in which these octahedra are aligned relative to a perfectly cubic arrangement is described using the Glazer notation^{34,35}. Filip et al. investigated the manner in which the A-site cation influences the structure of the PbI_6 based perovskite and hence the band gap. Different A site cations were tested, ranging from small atomic ions to larger ions, including various organic ions. The structure of the perovskite is modified by the effective size of the ion, the anisotropy of the ion, the steric hindrance of the ion, and intermolecular bonding such as hydrogen bonding. Perovskites incorporating atomic ions smaller than Cs were found to be less stable and decomposed into their constituent reagents^{18,32}.

There have been numerous studies using *ab initio* techniques and molecular dynamics to gain an understanding of the structure of MALI. In particular, effort has been directed at understanding the

influence of the organic MA cation on the perovskite structure and how this gives rise to the different phases of MALI. Methylammonium forms significant interactions – hydrogen bonds – between its amide hydrogen atoms, and the iodide ions. The influence of these interactions is to further distort the Pb-I-Pb interactions, altering bond angles, and in turn influencing the band gap of the material. There is potential for tuning the material through modification of both the shape of the MA cation and the number of hydrogen bonds that it forms. Furthermore, the dipole on the MA ion will influence both the long and short range ordering of the cations, which in turn will affect the perovskite octahedral arrangements³⁶. Lee et al. studied the strength of the hydrogen bonding by systematically looking at the ease by which the amine, methyl, or the entire MA cation, rotates within the perovskite. The shortest H-bond interaction occurs between an amine hydrogen and an iodide ion, assuming that there is head-to-tail alignment of the organic ions and that the tilt of the perovskite octahedral is strongly correlated with the strength of the hydrogen bonds. Phase changes induced by increasing temperature are detected by the change in dielectric permittivity, which shows a sharp jump on changing from the orthorhombic to tetragonal structure³⁷. Chen et al. demonstrated the dynamic behaviour of the MA ion within the three phases and the role it plays in the charge carrier diffusion rates and recombination³⁸. At lower temperatures in the orthorhombic phase, the rotation of the C-N bond within the perovskite cage is frozen, whereas the rotation of the hydrogen atoms about their respective C and N atoms is not. The influence of heating on the MALI structure, and the MA ion disorder is further demonstrated by Weller et al. and confirms the importance of hydrogen bonding³⁹.

The disorder of the MA ion has been modelled using Monte Carlo methods⁴⁰, where the dynamics of the MA rotation is not explicitly modelled, but instead particular “jumps” from one alignment within the cuboctahedron cage to another are considered. To control the probability of these jumps occurring, the simulation determines the energy change caused by the change in dipole-dipole interactions between the MA ions, and the induced strain energy caused by the realignment of an ion. It was shown that, depending on the magnitude of the strain energy, the simulation would form either spontaneously antiferroelectric or ferroelectric domains as the simulation was cooled. Strain energy was defined as the energy change when rotating a MA ion by 180° from facing one side of the cubic cell, to the opposite, while all other MA ions within the simulation are aligned head-to-tail facing in the original direction. When the strain energy was 25 meV the simulated MALI upon cooling formed alternating layers, giving rise to an antiferroelectric material. But with a higher strain energy of 50 meV the MALI would form ferroelectric domains. Furthermore, it has been shown that care must be taken when interpreting simulations and the ordering that occurs, as periodic boundary conditions and Γ sampling will influence the stability of MA ion alignments⁴¹, which in turn has an influence on the relaxation times for the MA ions. Based upon their simulations and extrapolations, a relaxation time for the MA ion rotations was determined to be 10.4 ps. *Ab initio* molecular dynamics simulations suggest that the MALI material is like an orientational glass, with frustrated cation interactions. However, the ability of an *ab initio* simulation to assess the long-range orientational correlations is hampered by the limited size of the simulated supercell.

Ab initio molecular dynamics simulations have also been used to investigate the thermal effects upon the MALI structure and the band gap. In order to perform the simulations, the supercells were limited to a 3x3x3 construction from the unit cells, or smaller. These fully dynamic simulations established that the ordering of the MA ions depends upon the hydrogen bonding the MA ion participates in, with relaxation times for the MA ion determined to be approximately 1.5 ps for a 3x3x3 supercell, or 17.5 ps for the smaller 2x2x2 supercell, with periodic boundary conditions being cited as the reason why long range interactions were too strongly correlated to the MA ion rotations. The band gap of MALI was found to vary with a standard deviation of 0.113 eV over the course of the simulation. However, a supercell simulation consisting of 2x2x2 unit cells is insufficient to model the disorder of the MA ions properly.

The significance of the hydrogen bonding to the structure has been examined by Lee et al.⁴² Using DFT calculations, various orientations of the MA ion in the cuboctahedron cage have been compared in terms of energetic stability, hydrogen bond distances and also by performing a topological analysis of the electron density – following the method of discussed in^{43,44}. Two main modes of hydrogen bonding motifs are identified, and their influence on the MALI band gap is determined. The α form, where two hydrogen bonds are formed between the amine group hydrogens and the iodide ions, results in a bandgap of 1.73 eV, while the β form, where only one of these hydrogen bonds is formed, gives rise to a bandgap of 2.03 eV. Bonding energies and bond lengths are compared to the electron density found at the hydrogen bond critical points, with the hydrogen bonding satisfying the trends for hydrogen bonds in other materials.

Most simulations of MALI have been performed using DFT. The only example of a classical potential for MALI that we have found is the MYP potential of Mattoni et al.⁴⁵ Within this potential the interactions between the atoms that make up the MA ion are governed by the potentials and parameters taken from the AMBER force field. A Buckingham potential is used to describe the interactions between the lead and iodide ions. The potential for determining the interactions between the inorganic and organic ions of MALI is less typical, and uses a combination of Buckingham potential and Lennard-Jones 12-6 potential, along with a standard Coulombic interaction term. The initial potential parameters were developed for CsPbI₃, which in turn was a rescaling of parameters for a MgSiO₃ potential. The potential is able to recover the phase transitions with increasing temperature, and also to demonstrate the ordering of the MA ions, and the loss of this ordering as the temperature of the simulation is increased. However, the charges assigned to the atoms in the MYP potential are larger than the standard valence charges of the constituent ions, which is inconsistent with the suggestion of this material exhibiting a degree of covalency. Furthermore, the size of the charges makes the potential incompatible with many other inorganic and organic potentials, which impedes its transferability beyond the MALI perovskite to other mixed hybrid metal organic perovskites and their precursors limiting the use of this potential model.

Even though the corner sharing octahedral motif is fundamental to the perovskite structure, and to the band gap itself, very little effort has been focused on understanding how the signature perovskite cage of the materials forms, given that the perovskite can be synthesised by simply grinding together the two constituent

precursor materials^{46,47}. This means that PbI₂, a layered material consisting of planes of edge sharing PbI₆ octahedra, readily incorporates MA ions, and changes from an edge-sharing configuration to a corner-sharing structure. Understanding the mechanism of this reaction is of critical importance, given how sensitive MAPbI₃ synthesis is to the processing conditions, such as the presence of water.

We present a new forcefield that has been designed to be transferable, and to simulate both the reactants and the products when forming MALI.

Methods

Simulation Details

All reference structures used for fitting were obtained either from XRD data, or generated by simulation. Simulations were performed using Density Functional Theory calculations using CASTEP 16.0⁴⁸. The PBE functional was used with on-the-fly pseudopotentials with a cut-off energy of 700 eV (determined to be sufficient following cut-off energy convergence testing) and a convergence tolerance of 1×10^{-5} . The systems were fully geometry relaxed using the BFGS method. Convergence criteria were set at 0.005 eV (energy), 0.1 eV (forces), 0.1 eV (stress), and 0.05 eV (displacement). A single gamma point was used and found sufficient for the size of the simulation box. Dispersion interactions are accounted for by the Tkatchenko-Scheffler method⁴⁹.

All molecular dynamics simulations were performed using DL_POLY⁵⁵. The simulations used 0.5 fs time steps. NVT ensemble simulations used the Berendsen thermostat with a relaxation time of 0.001 ps, and NPT simulations were performed with the Hoover thermostat (relaxation time 0.001 ps) and barostat (relaxation time of 0.1 ps). All simulations utilised the Ewald summation for electrostatic interactions, with a precision of $1.0 \times 10^{-6} \text{ \AA}^{-1}$. All simulations used the Verlet algorithm. For the determination of the auto-correlation functions, simulation time steps of 0.05 fs were used.

Defect calculations were all performed in GULP⁵³ using the Mott-Littleton method. The inner region around the defect, within which atoms are all freely able to relax, used an initial cut-off of 15 Å. The outer region within which only short-range interactions and Coulombic interactions are considered, used an initial cut-off of 55 Å. Defect energies were tested for convergence by increasing both region cut-offs by a 1 Å increment at the same time.

Potential Development

Potential Model Selection

The potential consists of two core parts; the organic molecule, which uses functions and parameters taken from the GAFF force field, and the inorganic part that models the interactions between lead and iodide, derived from the potential developed by Winkler⁵⁰. New functions have been fitted to model the interactions between the organic cation and the lead and iodide ions. This is where the fitting of the potential parameters has been focused.

While the GAFF force field is well known and studied for biochemical simulations⁵¹, the Winkler model for lead iodide is less well known. The Winkler model uses Buckingham type potentials to model the interactions between the ions, and includes polarisation

ARTICLE

Journal Name

effects via a shell model. We have modified this potential for simplicity, and removed the tethered charges on springs, and the ionic charges are now the sum of their previous nuclei charge and the charges on their associated spring.

To account for the interactions between the organic cation and the lead and iodide ions, Lennard-Jones potentials were fitted, with the aim of reproducing key features of the structure and the material. In particular, the lattice parameters for MALI, and the phonon density of states were important guides to the fitting procedure. Confirmation of the quality of the fit was also revealed through molecular dynamics simulations, where phase changes were explored as the simulation was increased in temperature, as a fundamental test of the transferability of the potential.

Potential Fitting

Typically, the combining of inorganic and organic potentials is hampered by the disparity of the charges used in the two potentials, which causes unrealistic Coulombic interactions between the inorganic ions and the organic molecule atoms. This can be corrected by rescaling the inorganic ion potential to account for the rescaling of the inorganic ion charges. However, in the case of the Winkler potential, the lead and iodide charges – determined as a summation of the original nuclei charges and the shell charge, are comparable in magnitude to those of the organic atoms. After coalescing the nuclei and shell charges of lead and iodide, the Buckingham potential parameters for this potential had to be refitted. The Buckingham potential consists of three parameters, A, ρ , and C, which represent the size of the close range repulsive barrier, the length of the repulsive region, and the magnitude of the attractive dispersion interaction. In total nine parameters were adjusted in order to return the bulk lead iodide structure for the 2H polytype.

The parameters for the methylammonium cation were taken from the GAFF forcefield and generated using the ANTECHAMBER application and were unmodified⁵².

Following this procedure means that the MALI potential is equally capable of simulating the reactants individually, rather than resulting in potentials and parameters that have been overfitted to give a model capable of simulating only the MALI bulk material and not the surface, defects and formation of MALI.

To account for the interactions between the MA cation and the lead and iodide ions, Lennard-Jones terms have been included, in the “12-6” form. The Lennard-Jones potential consists of two parameters, A and B. A determines the magnitude of the close range repulsion, while B determines the magnitude of the long range dispersive attraction. In order to obtain an appropriate starting point for these parameters Lennard-Jones potentials were fitted to the potential energy curves for lead and iodide obtained from the Winkler potential. Then, using the Lorenz-Berthelot mixing rules, Lennard-Jones potentials were generated for the interactions between the lead and iodide ions, and the four atoms types of the MA cation – the hydrogen atoms attached to the carbon atom are chemically different to those attached to the nitrogen atom. With these eight new sets of Lennard-Jones parameters, the force field could then be fitted to reproduce the structure and phonon density of states for MALI.

Parameterisation was performed, and tested against increasing the supercell size, using the GULP program⁵³. The increase in the size of the supercell is accompanied by increased flexibility of the system as more of the octahedra are strung together. In the smaller systems, and where an odd number of octahedra span the supercell, the tilting of the octahedra can become frustrated and not representative of the real system.

Table 1 Parameterisation

Buckingham Potentials ($A \exp(-\rho/r) - C/r^6$)					
		A (eV)	ρ (Å)	C (eV Å ⁻⁶)	
Pb	I	6876.2	0.32367	510.0	
Pb	Pb	17032.7	0.285	1100.19	
I	I	1791.81	0.46529	470	
Lennard-Jones 12-6 Potential ($X/r^{12} - Y/r^6$)					
		X (eV Å ⁻¹²)	Y (eV Å ⁶)		
Pb	C	100000.89	121.072		
Pb	N	90000.60	131.856		
Pb	H1	1435.31	8.789		
Pb	H2	3590.72	16.445		
I	C	15180.13	0.743		
I	N	40465.16	0.809		
I	H1	1134.51	0.054		
I	H2	942.79	0.025		
C	C	45262.52	29.32		
C	N	43197.02	31.98		
N	N	40975.84	34.77		
C	H1	986.76	2.66		
C	H2	111.38	0.90		
N	H1	875.63	2.80		
N	H2	92.25	0.91		
H1	H1	8.76	0.15		
H1	H2	0.40	0.033		
H2	H2	0.006	0.004		
I	H2	1142.79	0.025		
Two Body Potentials ($\frac{1}{2}k(r-r_0)^2$)					
		k (eV Å ⁻²)	r ₀ (Å)		
C	N	25.480	1.499		
C	H1	29.395	1.091		
N	H2	32.024	1.033		
Three Body Potentials ($(k/2)(\theta-\theta_0)^2$)					
			k (eV)	θ_0 (°)	
N	C	H1	4.254	108.0	
C	N	H2	4.009	110.11	
H1	C	H1	3.388	110.74	
H2	N	H2	3.517	108.11	
4 Body Potentials ($A[1+\cos(m\phi-\delta)]$)					
			A (eV)	δ (°)	m
H1	C	N	0.00675	0.0	3
Charges					
			q		
Pb			1.263		
I			-0.632		
C			0.072		
N			-0.832		
H1			0.058		
H2			0.405		

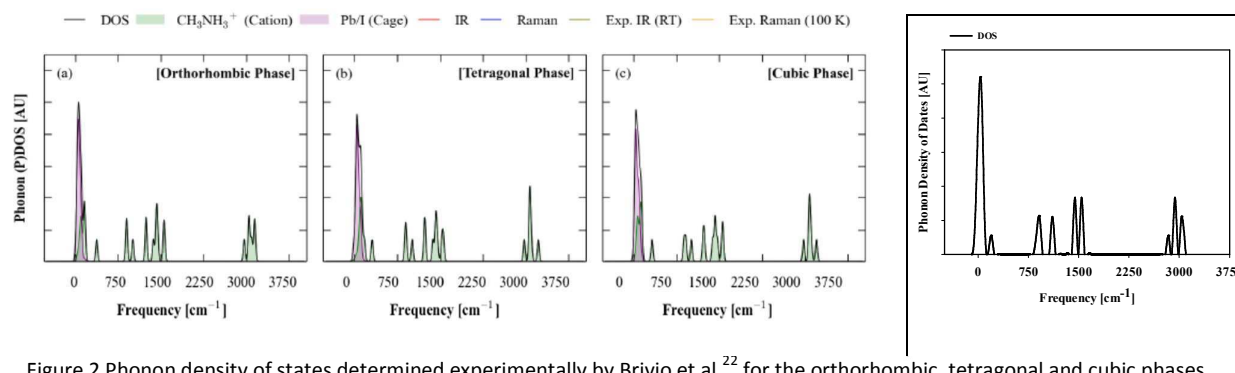


Figure 2 Phonon density of states determined experimentally by Brivio et al.²² for the orthorhombic, tetragonal and cubic phases, and on the far right, the computational determined phonon density of states from the force field.

Results and Discussion

An initial guide to the quality of the fit, beyond the lattice parameters, is the phonon density of states (DOS), figure 2. Our parameterisation provides good qualitative fits to the experimentally derived DOS, with key peaks reproduced²². The bulk modulus has an average value of 13.62 GPa, which is comparable to the value of 13.9 GPa as determined by Rakita et al.⁵⁴ The Shear Modulus was also determined by Rakita et al. to be 5.4 GPa, compared to our calculated value of 7.28 GPa.

Molecular dynamics Simulations were initially run at 400K for 0.3 ns and then quenched. The initial 5000 steps were discarded as the simulations approached equilibration. Simulations were initially performed using the NVT regime and then final simulations were performed with the NPT regime.

From table 2 it is clear that there is an increase in the volume as temperature increases, but no significant change in the lattice angles or in the ratio between the lattice parameters. This does not suggest any phase change from orthorhombic to tetragonal, as reported by Mattoni et al.⁴⁵. However, our room temperature lattice parameters are in good agreement with experiment⁵⁶ and produce a similar cell volume. We have explored the lattice parameters themselves, for simulations at 300K, with small increases in decreases in a , b , and c , or through small deviations away from 90 for each of α , β , and γ , however in all cases, the lattice parameters returned to the same average optimal values suggesting this is the preferred structure.

The phase changes reported have primarily been linked to a change in the tilt of the octahedral as the system and a shift in the ordering of the methyl ammonium cations. Therefore to further investigate the influence of temperature on the phases we have examined the structure at a range of temperatures. These show an obvious change in structure as the system is heated, and this can be shown using radial distribution functions (RDF), and simply by looking at snap shots of the structure. Figures 3-6 show the structure of the simulation, looking down the c -axis. Figure 3, from a simulation at 300K shows significant disorder, both for the octahedra tilts, octahedra shapes, and the orientations of the methylammonium cations. Figures 4-6 are from a simulation at 50K. There is clearly ordering of the methylammonium cations, and the octahedra have more regular tilts and shapes. Many layers show the same tilt arrangement, but this can reverse, and continue, for a number of layers. The MA cations can also have domains of alignment.

The RDF for the C-C interactions, figure 7, shows that at low temperature there is ordering, which is related to the arrangement of the MA cations in neighbouring cuboctahedra aligning head to tail, head to head, or orthogonally. As the temperature is increased, the distance between the C-C atoms on average is increased as the system expands, and much of the structure in the RDF is lost, as the MA cations become more able to tumble and rotate within the cuboctahedra cavities. This is why the peak at 7.7 Å is lost, and the shortest C-C distance on average increases from 6 Å, to 6.5 Å. The fine structure, and so the short and long range ordering present in MAlI, is removed once a temperature of >150K is achieved, which falls in line with the phase transition seen at that temperature. In the RDF for the iodide-methyl hydrogen atom distances, figure 8, we also see again a shift to longer distances for the peaks, and the loss of fine structure such as the shoulder in the first peak. The shoulder is due to the fact that at low temperature, while there is one close range I-H interaction, there are two more methyl hydrogen atoms. The shift in peak distance, broadening, and loss of the shoulder at higher temperatures, reflects that the MA cation then occupies a more central position, and is able to freely rotate. The peaks around 6.5 Å, 8 Å and 9 Å, which correspond to the methyl hydrogen atoms interacting with the other iodide ions that make up the cubo-octahedron occupied by the MA cation, clearly shift and merge with increasing temperature, and this can be related to the loss of octahedral tilt of the PbI_6 subunits. Therefore our model appears to replicate the atomic relaxations observed during the phase changes within this material. We do not observe any phase change between 300 K and 400 K (identified as tetragonal to cubic).

Table 2 Average Simulation Lattice Parameters and Structure Data

Lattice Parameters	Temperature						Experiment 293K ⁵⁶
	50K	100K	150K	200K	250K	300K	
$a/\text{Å}$	8.79	8.66	8.68	8.71	8.74	8.79	8.90
$b/\text{Å}$	8.98	8.85	8.88	8.90	8.94	8.98	8.90
$c/\text{Å}$	12.56	12.39	12.42	12.46	12.50	12.56	12.67
$\alpha/^\circ$	88.25	88.25	88.25	88.25	88.25	88.25	90.0
$\beta/^\circ$	90.00	90.00	90.00	90.00	90.00	90.00	90.0
$\gamma/^\circ$	90.00	90.00	90.00	90.00	90.00	90.00	90.0
Volume/ Å^3	941	949	957	966	976	991	1000
Volume change/ Å^3	-	8.3	15.8	24.9	35.0	49.8	
c/a	1.43	1.43	1.43	1.43	1.43	1.43	1.42
a/b	0.98	0.98	0.98	0.98	0.98	0.98	1.0

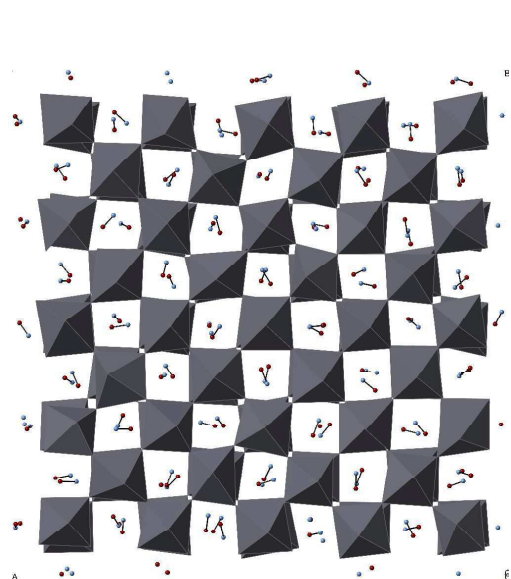


Figure 3 Snapshot of MALI simulation of a 5x5 supercell, at 300K. Methylammonium cations are represented as just C-N rods to better see the lack of ordering.

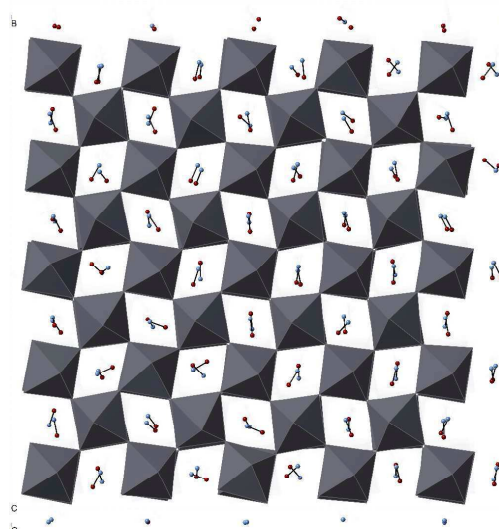


Figure 5 A slice through a snapshot of MALI simulation of a 5x5 supercell, at 50K. Methylammonium cations are represented as just C-N rods to better see the ordering that emerges on quenching the simulation from 400K. The direction of the tilt has interchanged with respect to the layers in figure 4.

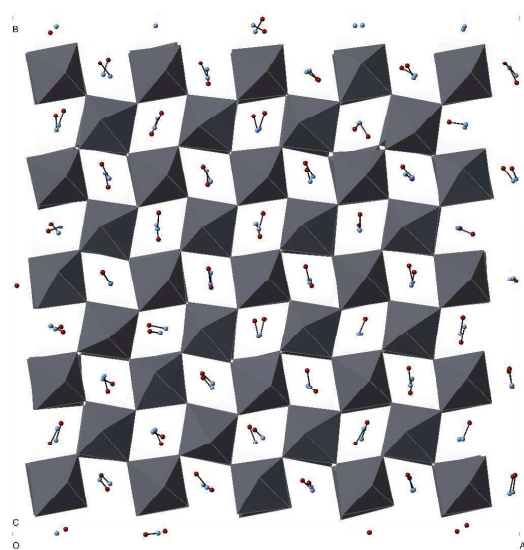


Figure 4 A slice through a snapshot of MALI simulation of a 5x5 supercell, at 50K. Methylammonium cations are represented as just C-N rods to better see the ordering that emerges on quenching the simulation from 400K.

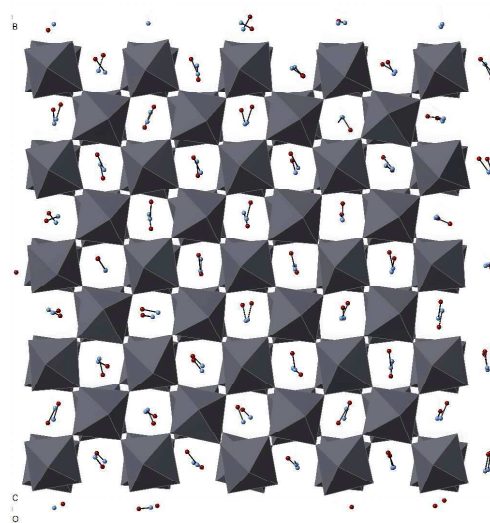


Figure 6 A slice through a snapshot of MALI simulation of a 5x5 supercell, at 50K. Methylammonium cations are represented as just C-N rods to better see the ordering that emerges on quenching the simulation from 400K. The interface between layers is seen where the direction of the tilt interchanges.

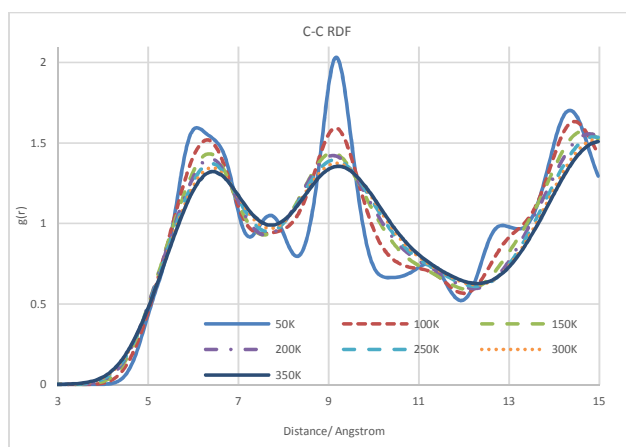


Figure 7 Radial Distribution Function for C-C interactions between MA cations

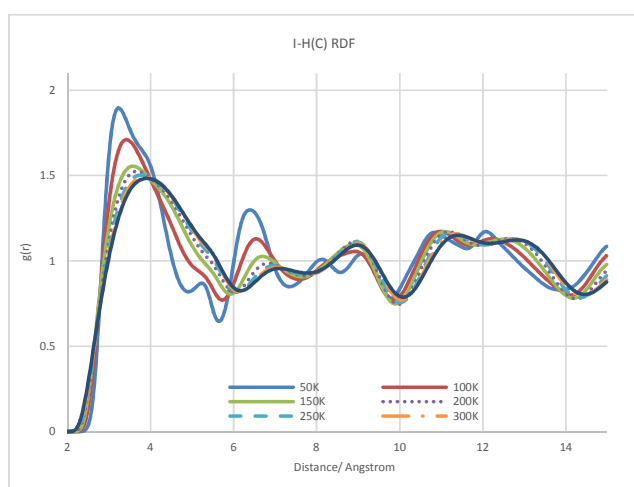


Figure 8 Radial Distribution Function for the I-H(C) interactions. H(C) are hydrogens atoms attached to the methyl group carbon atom.

We can further probe the accuracy of our model by examining the strength of the hydrogen bonding by extracting the rotational relaxation times for the MA cations.

$$C(t) = \left\langle \sum_{i=1}^N \vec{\mu}_i(t) \cdot \vec{\mu}_i(0) \right\rangle$$

$$C(t) = \frac{1}{N} \sum_{i=1}^N \langle \cos \theta_i(t) \rangle$$

In equation 2, the autocorrelation function, $C(t)$ at a time t , is determined as the ensemble average of the dot product of the dipole vector at time t and the dipole vector at time $t=0$. Given that any point in our simulations can be used as starting point, we can then further average over the entire simulation.

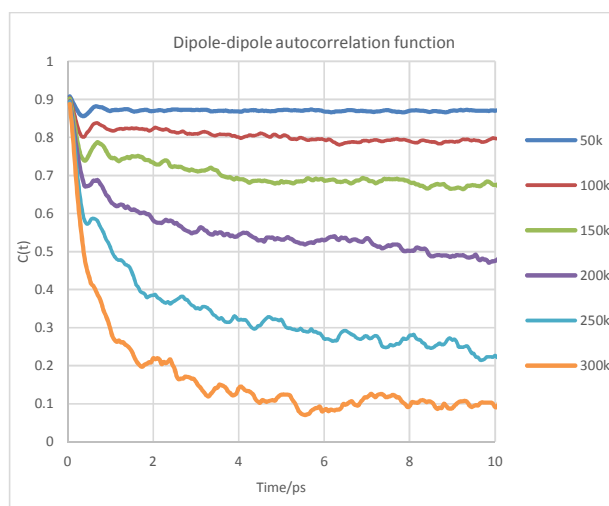


Figure 9 Plots of the Dipole Autocorrelation Function at different temperatures.

From the plot of the autocorrelation function, figure 9, it is clear that, at low temperatures, the direction that the MA cations point in is highly correlated with their orientation over time. The autocorrelation dies away quickly as temperature increases, and there is more dramatic change as the material is simulated at temperatures above 150 K, which is a temperature that coincides with an experimentally observed transition state. Compared to the work of Mattoni et al. the autocorrelation function is not as strongly influenced by increasing temperature⁴⁵.

From these curves we can extract the rotational relaxation time, which is a measure of how long it takes for the system to evolve and become disordered, relative to a starting configuration.

$$C(t) = ae^{-\frac{t}{\tau_0}} \#3$$

$$C(t) = e^{-\frac{t}{\tau_0}} \left[A + \frac{t}{\tau_0} e^{-\left(\frac{t}{\tau_1}\right)^2} + (1-A) \cos\left(\frac{2\pi t}{\tau_2}\right) \frac{1}{\left(\frac{t}{\tau_3} + 1\right)^3} \right] \#4$$

Equations 3 and 4 represent two different approaches to extracting the relaxation time, τ_0 . Whereas equation 3 assumes a simple exponential decay, equation 4 assumes a more complex form where dipole alignments correlations are represented by the #2 inclusion of a cosine term⁵⁷.

From equation 3, τ_0 is found to be 1.860 ps, which is much faster than that determined experimentally for MALI. Using equation 4, we extract a value 7.15 ps which agrees well with the experimental values of 14 ps⁴⁰, and 4.70 ps³⁸, suggesting our parameterisation is correctly modelling the rotational dynamics of the MA cations.

We have briefly investigated the intrinsic vacancies that occur in the MALI cell using our potential. The values are listed in table 3.

In all cases convergence is achieved to a satisfactory level that allows difference defects to be compared. A more rigorous defect examination using supercells, defect clusters and variability in the ideal lattice is beyond the scope of this paper and will be

ARTICLE

Journal Name

considered in future work. We particularly note that in all our calculations the MA cations are all aligned head to tail.

Defects I1, I2, and I3 refer to different Iodide positions relative to the MA cation. I1 and I2 reside at the ends of the molecule while I3 is in a position equatorial to the MA N-C bond vector, all the Pb atoms are equivalent with respect to the MA cation.

As can be seen from table 3 the defect energies for the I sites are all very similar. The MA vacancy is the most favourable defect with a value close to that of the Iodides while the Pb vacancy is much less favourable. The values compare well with those of Yin *et al.*⁵⁸ except the energy of formation of the Pb defect is much larger in our model. We would expect differences in the absolute values due to the differences in methodology. The trend in defect energies is also in agreement, with the formation of Pb defects costing more energy than forming MA or I defects, both of which have similar energies of formation.

Table 3 Average Defect Energies of Formation

Defect	Energy/ eV
I1, I2, I3	1.87, 1.93, 1.91
MA	1.43
Pb	8.21

The presence of defects does have an influence on the structure, in particular the removal of an iodide ion results in the reorientation of MA cations (figure 10). The iodide defects also induce a structural change, where in phase tilting changes to be out of phase tilting, figure 11. However, this again, is only in the case of an optimization of the structure about a defect.

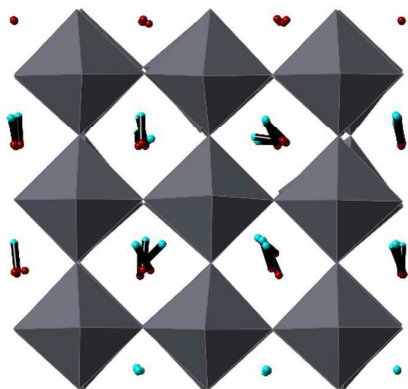


Figure 10 A section of the Mott-Littleton simulation, centred on the Pb defect. Pictured are three layers of octahedra, hence why the defect is hidden. MA cations are represented as blue nitrogen atoms, and red carbon atoms.

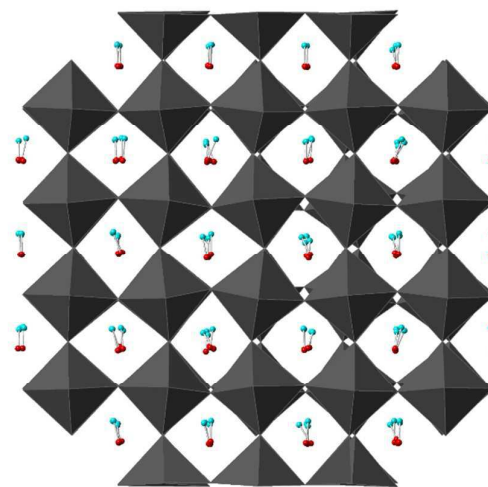


Figure 11 A section of the Mott-Littleton simulation, centred on the I3 defect. Pictured are three layers of octahedra, hence why the defect is hidden.

Conclusions

We have created a new forcefield that enables the simulation of MALI. The forcefield is designed in a manner that allows the greatest amount of transferability, in particular the forcefield utilizes existing functions and parameters for the reactants, lead iodide and methylammonium iodide. We have shown that adding functions to describe the short-range repulsion and long range attraction between the lead and iodide ions, and the MA cation results in a forcefield that returns qualitatively the expected MALI crystal structure, and phonon density of states. Our forcefield also demonstrates accurate behaviour in the cation dynamics which are fundamental to the functionality of this material. We briefly examine the relative stability of single ion vacancy defects, and their influence on the optimized structure.

Acknowledgements

We would like to thank Prof John Harding for helpful discussions. We would also like to thank Whitney Schimdt for her advice as a synthetic materials scientist. Funding was provided under grant (EP/L017563/1). Via our membership of the UK's HEC Materials Chemistry Consortium, which is funded by EPSRC (EP/L000202), this work used the ARCHER UK National Supercomputing Service (<http://www.archer.ac.uk>).

- 1 *Science*, 2013, **342**, 1438–1439.
- 2 N.-G. Park, *Mater. Today*, 2015, **18**, 65–72.
- 3 *Nature*, 2013, **504**, 357–365.
- 4 J. Cui, H. Yuan, J. Li, X. Xu, Y. Shen, H. Lin and M. Wang, *Sci. Technol. Adv. Mater.*, 2015, **16**, 36004.
- 5 B. O'Regan and M. Grätzel, *Nature*, 1991, **353**, 737–740.
- 6 H.-S. Kim, C.-R. Lee, I.-H. Jang, W.-K. Kang and N.-G. Park, *Bull. Korean Chem. Soc.*, 2012, **33**, 670–674.
- 7 L. Schmidt-Mende, S. M. Zakeeruddin and M. Grätzel, *Appl. Phys. Lett.*, 2005, **86**, 13504.
- 8 D. Weber, *Z Naturforsch*, 1978, **33b**, 1443–1445.

- 9 J.-H. Im, C.-R. Lee, J.-W. Lee, S.-W. Park and N.-G. Park, *Nanoscale*, 2011, **3**, 4088–4093.
- 10 H.-S. Kim, C.-R. Lee, J.-H. Im, K.-B. Lee, T. Moehl, A. Marchioro, S.-J. Moon, R. Humphry-Baker, J.-H. Yum, J. E. Moser, M. Grätzel and N.-G. Park, *Sci. Rep.*, 2012, **2**.
- 11 M. M. Lee, J. Teuscher, T. Miyasaka, T. N. Murakami and H. J. Snaith, *Science*, 2012, **338**, 643–647.
- 12 A. Kojima, K. Teshima, T. Miyasaka and Y. Shirai, *Meet. Abstr.*, 2006, **MA2006-02**, 397–397.
- 13 A. Yella, H.-W. Lee, H. N. Tsao, C. Yi, A. K. Chandiran, M. K. Nazeeruddin, E. W.-G. Diao, C.-Y. Yeh, S. M. Zakeeruddin and M. Grätzel, *Science*, 2011, **334**, 629–634.
- 14 J. Burschka, A. Dualeh, F. Kessler, E. Baranoff, N.-L. Cevey-Ha, C. Yi, M. K. Nazeeruddin and M. Grätzel, *J. Am. Chem. Soc.*, 2011, **133**, 18042–18045.
- 15 A. Poglitsch and D. Weber, *J. Chem. Phys.*, 1987, **87**, 6373–6378.
- 16 N. Mercier, N. Louvain and W. Bi, *CrystEngComm*, 2009, **11**, 720–734.
- 17 C. Li, X. Lu, W. Ding, L. Feng, Y. Gao and Z. Guo, *Acta Crystallogr. Sect. B*, 2008, **64**, 702–707.
- 18 A. Amat, E. Mosconi, E. Ronca, C. Quarti, P. Umari, M. K. Nazeeruddin, M. Grätzel and F. De Angelis, *Nano Lett.*, 2014, **14**, 3608–3616.
- 19 R. D. Shannon, *Acta Crystallogr. Sect. A*, 1976, **32**, 751–767.
- 20 B. N. Cohen, C. Labarca, N. Davidson and H. A. Lester, *J. Gen. Physiol.*, 1992, **100**, 373–400.
- 21 J. M. Frost, K. T. Butler, F. Brivio, C. H. Hendon, M. van Schilfegaarde and A. Walsh, *Nano Lett.*, 2014, **14**, 2584–2590.
- 22 F. Brivio, A. B. Walker and A. Walsh, *APL Mater.*, 2013, **1**, 42111.
- 23 Y. Yamada, T. Nakamura, M. Endo, A. Wakamiya and Y. Kanemitsu, *Appl. Phys. Express*, 2014, **7**, 32302.
- 24 V. D’Innocenzo, G. Grancini, M. J. P. Alcocer, A. R. S. Kandada, S. D. Stranks, M. M. Lee, G. Lanzani, H. J. Snaith and A. Petrozza, *Nat. Commun.*, 2014, **5**, 3586.
- 25 K. Tanaka, T. Takahashi, T. Ban, T. Kondo, K. Uchida and N. Miura, *Solid State Commun.*, 2003, **127**, 619–623.
- 26 L. Gil-Escrig, A. Miquel-Sempere, M. Sessolo and H. J. Bolink, *J. Phys. Chem. Lett.*, 2015, **6**, 3743–3748.
- 27 C. Quarti, E. Mosconi and F. D. Angelis, *Phys. Chem. Chem. Phys.*, 2015, **17**, 9394–9409.
- 28 M. R. Filip and F. Giustino, *Phys. Rev. B*, 2014, **90**, 245145.
- 29 P. Pyykko, *Chem. Rev.*, 1988, **88**, 563–594.
- 30 E. Mosconi, A. Amat, M. K. Nazeeruddin, M. Grätzel and F. De Angelis, *J. Phys. Chem. C*, 2013, **117**, 13902–13913.
- 31 J. Even, L. Pedesseau, J.-M. Jancu and C. Katan, *J. Phys. Chem. Lett.*, 2013, **4**, 2999–3005.
- 32 M. R. Filip, G. E. Eperon, H. J. Snaith and F. Giustino, *Nat. Commun.*, 2014, **5**.
- 33 T. Baikie, Y. Fang, J. M. Kadro, M. Schreyer, F. Wei, S. G. Mhaisalkar, M. Graetzel and T. J. White, *J. Mater. Chem. A*, 2013, **1**, 5628–5641.
- 34 A. M. Glazer, *Acta Crystallogr. B*, 1972, **28**, 3384–3392.
- 35 A. M. Glazer, *Acta Crystallogr. Sect. A*, 1975, **31**, 756–762.
- 36 J.-H. Lee, N. C. Bristowe, P. D. Bristowe and A. K. Cheetham, *Chem. Commun.*, 2015, **51**, 6434–6437.
- 37 N. Onoda-Yamamuro, T. Matsuo and H. Suga, *J. Phys. Chem. Solids*, 1992, **53**, 935–939.
- 38 T. Chen, B. J. Foley, B. Ipek, M. Tyagi, J. R. D. Copley, C. M. Brown, J. J. Choi and S.-H. Lee, *Phys. Chem. Chem. Phys.*, 2015.
- 39 M. T. Weller, O. J. Weber, J. M. Frost and A. Walsh, *J. Phys. Chem. Lett.*, 2015, **6**, 3209–3212.
- 40 A. M. A. Leguy, J. M. Frost, A. P. McMahon, V. G. Sakai, W. Kockelmann, C. Law, X. Li, F. Foglia, A. Walsh, B. C. O’Regan, J. Nelson, J. T. Cabral and P. R. F. Barnes, *Nat. Commun.*, 2015, **6**, 7124.
- 41 J. Even, M. Carignano and C. Katan, *Nanoscale*, 2015.
- 42 J. H. Lee, J.-H. Lee, E.-H. Kong and H. M. Jang, *Sci. Rep.*, 2016, **6**, 21687.
- 43 R. F. W. Bader, *Atoms in Molecules: A Quantum Theory*, Clarendon Press, Oxford England : New York, New Ed edition., 1994.
- 44 P. L. A. Popelier, *Atoms in Molecules: An Introduction*, Prentice Hall, Harlow, 1 edition., 2000.
- 45 A. Mattoni, A. Filippetti, M. I. Saba and P. Delugas, *J. Phys. Chem. C*, 2015, **119**, 17421–17428.
- 46 D. Prochowicz, M. Franckevičius, A. M. Cieślak, S. M. Zakeeruddin, M. Grätzel and J. Lewiński, *J. Mater. Chem. A*, 2015, **3**, 20772–20777.
- 47 J. H. Heo and S. H. Im, *Nanoscale*, 2016.
- 48 S. Clark, M. Segall, C. Pickard, P. Hasnip, M. Probert, K. Refson and M. Payne, *Z. Für Krist.*, 2005, **220**, 567–570.
- 49 A. Tkatchenko and M. Scheffler, *Phys. Rev. Lett.*, 2009, **102**, 73005.
- 50 B. Winkler, M. T. Dove, E. K. H. Salje, M. Leslie and B. Palosz, *J. Phys. Condens. Matter*, 1991, **3**, 539.
- 51 J. Wang, R. M. Wolf, J. W. Caldwell, P. A. Kollman and D. A. Case, *J. Comput. Chem.*, 2004, **25**, 1157–1174.
- 52 J. Wang and P. A. Kollman, *J. Comput. Chem.*, 2001, **22**, 1219–1228.
- 53 J. D. Gale, *J. Chem. Soc. Faraday Trans.*, 1997, **93**, 629–637.
- 54 Y. Rakita, S. R. Cohen, N. K. Kedem, G. Hodes and D. Cahen, *MRS Commun.*, 2015, **5**, 623–629.
- 55 I. T. Todorov, W. Smith, K. Trachenko and M. T. Dove, *J. Mater. Chem.*, 2006, **16**, 1911–1918.
- 56 Y. Dang, Y. Liu, Y. Sun, D. Yuan, X. Liu, W. Lu, G. Liu, H. Xia and X. Tao, *CrystEngComm*, 2014, **17**, 665–670.
- 57 R. G. Gordon, *J. Chem. Phys.*, 1966, **44**, 1830–1836.
- 58 W.-J. Yin, T. Shi and Y. Yan, *Appl. Phys. Lett.*, 2014, **104**, 63903.